photonics

MDPI

Article

Study on the Performance Degradation Mechanism of Low-Light-Level Image Intensifiers in Humid and Hot Environments

Meng Zhu [1,*], Mengmeng Liu [1], Mingqian Xu [2], Ru Yao [2], Rongxuan Liang [2], De Song [2] and Weijun Chen [2]

[1] AVIC China Aero-Polytechnology Establishment, Beijing 100028, China
[2] School of Physics, Changchun University of Science and Technology, Changchun 130022, China
* Correspondence: 13693600403@163.com; Tel.: +86-136-9360-0403

Abstract

To analyze the performance stability of image intensifiers under humid and hot environments, this study systematically investigates the device performance degradation mechanism through a combination of natural exposure tests, humidity variation aging tests, disassembly analysis of failed samples, and a vacuum decay model. Experimental and simulated results reveal that moisture ingress in a humid and hot environment serves as the dominant factor governing the luminance gain stability of devices. Microscopic defects such as cracks, voids, and delamination phenomena existing at the sealing interface between ceramic rings and metal gaskets are the direct cause of moisture penetration. The attenuation of luminance gain accelerates significantly with increasing ambient humidity, demonstrating that water vapor is the primary driving factor for the environmental failure of devices. This study clarifies the attenuation mechanism of luminance gain for image intensifiers under humid and hot environments, providing a theoretical basis for the optimization of packaging processes and the improvement in environmental adaptability of image intensifiers.

Keywords: image intensifiers; luminance gain degradation; humid and hot environment; moisture ingress

1. Introduction

The image intensifier is a vacuum imaging device, which has the advantages of achieving 10^6 times luminance gain and fast shutter speed in the nanosecond to picosecond range [1–3], making it highly valuable for applications in fields such as low-light-level imaging, ultrafast imaging, and single-photon detection [4–6]. The image intensifier converts weak optical signals into photoelectrons via the photocathode, amplifies electrons through the micro-channel plate (MCP), and reproduces visible light on the phosphor screen [7]. Its overall luminance gain depends on the photoelectric conversion, electron amplification, and electro-optical conversion efficiencies of internal components. Luminance gain is one of the key indicators of image intensifiers [8]. It reflects the ability of image intensifiers to amplify received weak optical radiation, and also serves as an important criterion for evaluating the service life of the device [9]. However, with the increasing demand for stable, long-lasting imaging under ultra-low-illumination environments such as military reconnaissance, astronomical observation, and security surveillance, the long-term reliability of image intensifiers has become a key factor restricting equipment effectiveness [10].

North Night Vision Technology Co., Ltd. reported that the lifetime of second-generation image intensifiers decreases with increasing operating duration, alongside

Check for updates

Received: 18 June 2026
Revised: 6 August 2026
Accepted: 25 August 2026
Published: 27 August 2026

Copyright: © 2026 by the authors. Licensee MDPI, Basel, Switzerland. This article is an open access article distributed under the terms and conditions of the Creative Commons Attribution (CC BY) license.

pronounced reductions in MCP gain and photocathode sensitivity [11]. Nevertheless, the intrinsic mechanisms responsible remain merely conjectural [4]. Recently, the research on the storage life of image intensifiers has focused on the lifetimes of photocathodes, outgassing characteristics of the MCP [12–15]. For the photocathodes, several distinct processes lead to their quantum efficiency degradation, such as surface "poisoning," deviation from stoichiometry, ion back bombardment, electrolysis, and thermally activated decomposition [12]. Poisoning caused by surface reactions with residual gases such as O_2, CO_2, CO, and H_2O that persists even in the absence of illumination and current extraction is arguably the most important for photocathode storage systems in service today [13]. For the outgassing characteristics of the MCP, the diffusion behaviors of various gases in the MCP glass have been studied, and the outgassing rate decreases faster at higher MCP glass temperatures [14]. Therefore, after high-temperature outgassing treatment, the outgassing rate of residual gases can also decrease to an extremely low level. Studies have further shown that for electron vacuum devices, the leak characteristics of the tube shell are a key factor governing device lifetime. Paquet et al. explored the impact of internal components within ceramic packages on the vacuum sealing performance of uncooled focal plane array detectors, showing that micropores in the ceramic substrate can induce chronic leaks undetectable by helium mass spectrometer leak detectors—ultimately leading to irreversible device performance degradation [16]. For ceramic-packaged image intensifiers, gas leaks are also a major driver of vacuum degradation, which induces the performance degradation of image intensifiers due to the ceramic casting molds [17]. So, the reliability of image intensifiers under humid and hot environments may be affected by multiple physical and chemical damage mechanisms. One important risk might originate from packaging-related outgassing and moisture accumulation: an inherent drawback of hermetic packaging is its tendency to accumulate volatile substances and moisture, thereby creating a harsh microenvironment for the device [18]. The effect of humidity on equipment begins with the formation and influence of a thin liquid film on the outer surface. When the ambient humidity exceeds the critical relative humidity, a thin water film with a thickness ranging from tens of nanometers to micrometers can form on the equipment surface [19]. This thin liquid film serves as a critical medium for electrochemical corrosion and the adsorption of harmful substances [20]. Thus, under high-temperature and high-humidity conditions, the lifetime of image intensifiers is subject to more influencing factors, which also poses a severe challenge to the reliable storage and long-term operational readiness of this equipment.

Based on the tests of image intensifiers stored in humid and hot environments, this paper investigates the performance degradation mechanism. Firstly, the disassembly of failed samples identifies potential causes of device failure. Subsequently, leveraging the vacuum device leak theory, we develop a model describing the time-dependent evolution of the ceramic tube shell leak rate and internal device vacuum, to verify the dominant driver of vacuum degradation. Finally, test data are used to fit a formula relating environmental humidity to image intensifier luminance gain, quantifying luminance gain degradation behavior under humidity–heat conditions.

2. Experimental Methods and Theoretical Models

2.1. Experimental Methods

2.1.1. The Storage Environment of Devices for Natural Exposure Test and Humidity Variation Aging Test

The natural performance degradation test is conducted at the Xishuangbanna test station, which represents a typical hot-humid rainforest climate [21]. The third-generation image intensifiers (North Night Vision Technology Co., Ltd., Xi'an, China) (same batch

from the lab) are placed statically under a shelter (roofed but open-sided), which was not directly exposed to solar radiation or rain. The exposure duration was 24 months, from April 2023 to April 2025. The accelerated humidity variation aging tests are performed in a temperature–humidity chamber (Model HWSN-350, Shaoxing bowei Instrument and Equipment Co., Ltd., Shaoxing, China). The temperature is maintained at 65 °C, with two humidity conditions: high humidity (75% RH) and low humidity (5% RH).

2.1.2. Luminance Gain Measurement Methods

The luminance gain of image intensifiers was measured using a standard A-light source (Model YF 1000, Hangzhou Everfine Photo Info Co., Ltd., Hangzhou, China) to provide incident illumination on the photocathode. The output luminance from the phosphor screen was measured with a luminance meter (Model PR 880, Photo Research Inc., Chatsworth, CA, USA). The luminance gain GL of the image intensifier, in units of $cd \cdot m^{-2} \cdot lx^{-1}$, is defined as the ratio of the output luminance L_{out} to the incident luminance E_{in}, expressed as [22]:

$$G_L = \frac{L_{out}}{E_{in}} \tag{1}$$

All measurements are performed in a dark room at a controlled ambient temperature of 23 °C. The devices under test are allowed to stabilize at this temperature for at least 2 h prior to measurement. The incident illuminance is set to 1.0×10^{-4} lx, which simulates typical low-light conditions. For each device, luminance gain is measured three times consecutively, and the average value is recorded. The measurement uncertainty, determined by repeated tests on a reference device over five separate days, is approximately ±5% (relative standard deviation).

2.2. Simulation Model for Vacuum Degradation

During operation and storage, the vacuum level inside the image intensifier continuously decreases over time. Models describing the flow characteristics of small leak holes, outgassing characteristics in tube shells, as well as gas leak rate and internal vacuum performance were established.

2.2.1. Gas Flow Characteristics for Small Leak Holes

Gas flow in extremely small leak holes is primarily influenced by factors such as the diameter of the leak hole, gas density, and ambient temperature. According to the relevant literature and existing research findings [23], the flow rate of gas in leak holes is proportional to the pressure difference across the hole.

$$\frac{F}{\varepsilon A} = D_k \frac{\Delta p}{RTL} \tag{2}$$

$$D_k = \frac{d_{pore}}{3} \sqrt{\frac{8RT}{\pi M}} \tag{3}$$

In these formulas, F is the gas molar flow rate; ε is the membrane porosity; A is the area of exposed area; Δp is the pressure difference across the two ends; L is the length; R is the ideal gas constant; T is the absolute temperature; D_k is the Knudsen diffusion coefficient; d_{pore} is the diameter of the pore; and M is the molecular weight of the gas.

2.2.2. Outgassing Characteristics of Internally Dissolved Gases in Tube Shell Materials

The tube shell of an image intensifier is mainly composed of a Kovar metal ring and a ceramic ring. Ceramic materials outgas relatively quickly during high-vacuum processing. It is generally believed that after high-temperature vacuum treatment, the outgassing from

ceramic materials has a negligible effect on the internal vacuum level of the tube shell [24]. The outgassing of dissolved gases from metal materials is primarily hydrogen. For the outgassing of dissolved gases from metal materials [25], the desorption rate $q(t)$ of gas molecules from the metal surface can be obtained as:

$$q(t) = K, u^2 = \frac{D}{2}\left(\frac{\partial u}{\partial x}\right)_{x=0}, t \geq 0 \tag{4}$$

where K_r is the molecular recombination constant, D is the diffusion coefficient of hydrogen atoms, and u is the hydrogen atom concentration, expressed as u (x, t).

2.2.3. Relationship Between Tube Shell Gas Leak Rate and Internal Vacuum

During the manufacturing process of image intensifiers, the vacuum level can reach 10^{-5} to 10^{-8} Pa. However, during operation and storage, the vacuum level inside the image intensifier continuously decreases over time.

If Q (Pa·l/s) represents the volume of gas leaked per second, according to the ideal gas law, the change in the number of moles of gas leaked can be derived as:

$$n = \frac{PV}{RT} \tag{5}$$

And the gas leak rate Q can also be expressed as:

$$Q = \frac{d(PV)}{dt} = V\frac{dP}{dt} \ (Under\ constant\ volume\ conditions) \tag{6}$$

2.3. Relationship Between Water Vapor Concentration, Temperature, and Humidity

In practical environments, humidity can be equivalently converted to water molecule concentration. To quantify the concentration of water vapor, the concept of absolute humidity is introduced, which is defined as the mass of water vapor contained per unit volume of air. The formula for calculating absolute humidity is:

$$a = \frac{RH \times E}{R} \times \frac{M}{T} \tag{7}$$

where RH is the relative humidity (%), E is the saturation vapor pressure (Pa) at the given temperature, M is the molar mass of water (0.018 kg/mol), R is the gas constant (8.314 J/(mol·K)), and T is the absolute temperature (K). Absolute humidity, a, is directly proportional to the partial pressure of water vapor and is a direct physical quantity characterizing the water vapor content. The curve of water saturation vapor pressure as a function of temperature is plotted in Figure 1.

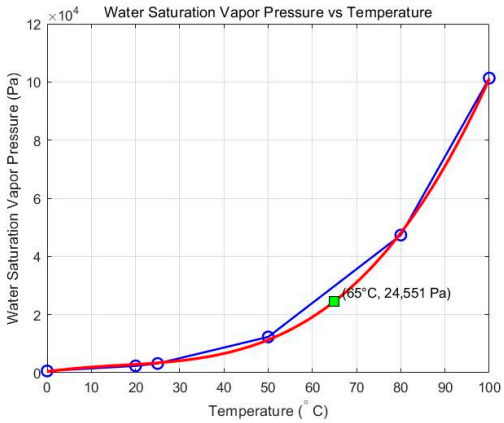


Figure 1. Fitted curve of water saturation vapor pressure as a function of temperature.

By fitting the data curve in Figure 1, the fitting formula for water saturation vapor pressure as a function of temperature is established as Equation (8), where T is the temperature in Kelvin and E is the saturation vapor pressure. Then, according to Equations (7) and (8), the water molecule concentration under different temperature and humidity conditions can be calculated.

$$E(T) = 0.1582 \times T^3 - 7.971 \times T^2 + 221.9 \times T + 359 \quad (8)$$

To facilitate comparison with experimental data, the absolute humidity a (g/m^3) is uniformly used to represent the water molecule concentration in the subsequent analysis. The calculation formula for water molecule concentration (absolute humidity a) is derived from the water vapor partial pressure and the ideal gas equation of state:

Water vapor partial pressure:

$$P_{H_2O} = RH \cdot E(T) \quad (9)$$

According to the ideal gas equation of state $PV = nRT$, the number of moles of water vapor per unit volume is:

$$C_{mol} = \frac{P_{H_2O}}{RT} = \frac{RH \cdot E(T)}{RT} \quad (10)$$

Then the absolute humidity (mass concentration of water vapor) is:

$$a = C_{mol} \cdot M = \frac{RH \cdot E(T) \cdot M}{RT} \left(\frac{g}{m^3} \right) \quad (11)$$

The number concentration of water vapor molecules is:

$$n_{H_2O} = C_{mol} \cdot N_A = \frac{RH \cdot E(T) \cdot N_A}{RT} \left(\frac{\text{number of molecules}}{m^3} \right) \quad (12)$$

where RH is the relative humidity (%); $E(T)$ is given by Equation (8): M = 0.018 kg/mol, R = 8.314 J/(mol·K), $N_A = 6.022 \times 10^{23}$ mol^{-1}, T is the absolute temperature (K).

3. Results and Discussion

3.1. Natural Performance Degradation Test

The measured data and normalized values of luminance gain of image intensifiers varying with exposure time, humidity, and temperature are presented in Table 1 and Figure 2, respectively. Except for Samples No. 3, No. 4, and No. 6, the luminance gain of the remaining products after 24 months of exposure remains above 70%. However, Samples No. 1 and No. 2 exhibit a clear degradation trend. The initial luminance gain of Sample No. 1 decreases from 12,500 $cd \cdot m^{-2} \cdot lx^{-1}$ to 8900 $cd \cdot m^{-2} \cdot lx^{-1}$, representing a degradation of 28.8%, essentially reaching the lifetime threshold. The initial luminance gain of Sample No. 2 decreased from 15,100 to 11,600 $cd \cdot m^{-2} \cdot lx^{-1}$, a degradation of 23.2%. The luminance gain of Sample 5 and Sample 9 fluctuates continuously. Following normalization, the gain oscillates around unity. A reduction in gain is observed under high temperature and humidity during storage, and vice versa.

Table 1. Luminance gain of the image intensifier ($cd \cdot m^{-2} \cdot lx^{-1}$).

Test Time (Months)	1#	2#	3#	4#	5#	6#	7#	8#	9#
	220,407	**210,326**	**220,442**	**210,046**	**220,445**	**210,033**	**220,444**	**220,416**	**220,408**
0	12,500	15,100	14,500	14,100	14,100	18,600	4500	13,800	15,300
6	10,300	10,900	-	-	12,500	10,400	3300	11,400	12,800

Table 1. *Cont.*

Test Time (Months)	1#	2#	3#	4#	5#	6#	7#	8#	9#
	220,407	**210,326**	**220,442**	**210,046**	**220,445**	**210,033**	**220,444**	**220,416**	**220,408**
12	8000	11,500	-	-	14,000	-	3000	11,200	12,600
15	9100	11,800	-	-	13,300	-	3100	12,700	15,500
18	8500	11,700	-	-	14,000	-	2800	12,300	14,700
24	8900	11,600	-	-	14,900	-	2540	12,500	15,300

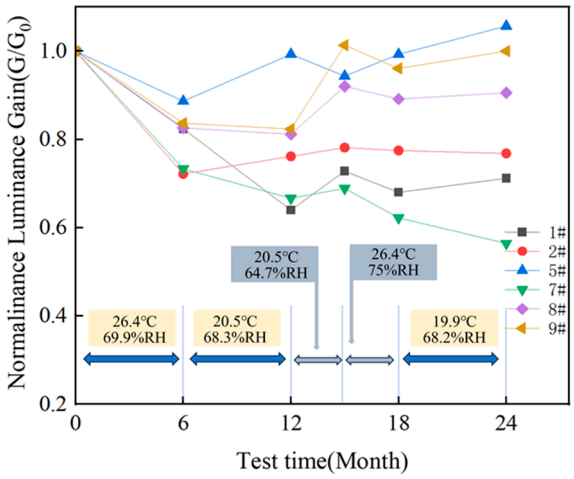
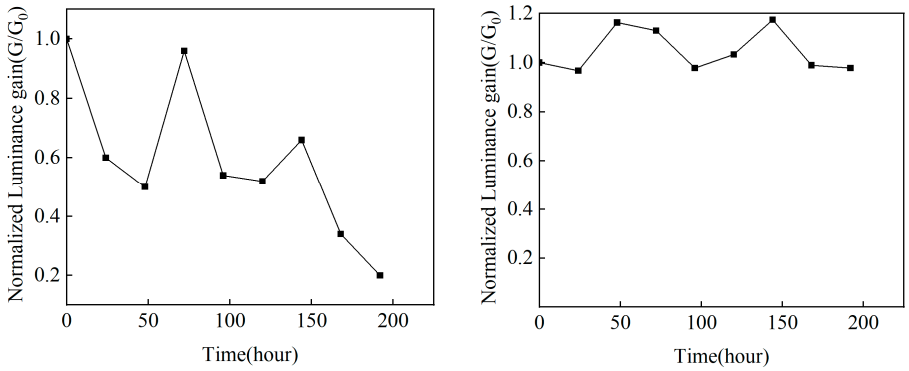


Figure 2. Normalized luminance gain of image intensifiers versus exposure time under humid and hot environments, together with the average temperature and humidity values corresponding to each storage stage (monitored every day by hygrothermograph).

3.2. Humidity Variation Aging Test

The degradation trend of luminance gain during the aging test of image intensifiers under different humidity levels is shown in Figure 3. To eliminate the influence of initial gain variation among devices, all measured gain values are normalized to their respective initial values. When the temperature is 65 °C and the humidity is 75%, the luminance gain exhibits a significant degradation over time. When the humidity is reduced to 5% while keeping the temperature and test duration unchanged, the luminance gain remains approximately constant. The test results indicate that ambient temperature has a relatively small effect on the luminance gain of the image intensifier, whereas ambient humidity causes a pronounced degradation of the luminance gain.



(**a**) 65 °C, 75% RH. (**b**) 65 °C, 5% RH.

Figure 3. Decay curve of normalized luminance gain over time during high-temperature high-humidity/low-humidity aging test (data from a single sample, No. 220406).

3.3. Disassembly and Analysis of Failed Samples

Based on the recorded results of luminance gain and failure phenomena of the field-exposed image intensifiers, failure/degradation mechanism analyses are carried out for three types of observed characteristics: (1) screen flickering and abnormal noise; (2) no image on the screen; (3) no obvious defect but gain performance degradation.

For the devices exhibiting screen flickering and abnormal noise, baking and retesting are performed, followed by disassembly inspection. It is found that the potting of the image intensifier (6#) had insufficient elastomer filling, resulting in voids and brittleness, as shown in Figure 4b,c. Figure 4a–c present photographs of the image intensifier tube shell before and after removal of its rigid outer housing. Figure 4d displays the power supply surface after removal of the sealing compound. These voids are located at the high-voltage solder joint, failing to provide adequate sealing and insulation protection for the bare tube and the solder joint. The severely aged area is highlighted by the red circle in the magnified view of Figure 4c. After prolonged moisture ingress, the surrounding elastomer ages and becomes brittle, and water stains accumulate at the void locations, ultimately leading to discharge at the high-voltage solder joint and causing flickering of the image intensifiers.

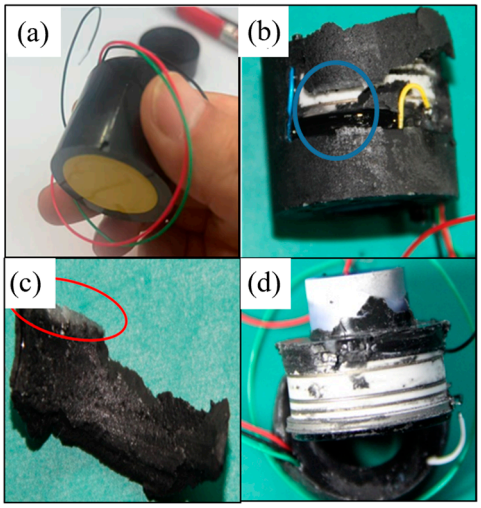


Figure 4. Photograph of image intensifier sample. (**a**) Intact sample with rigid outer housing; (**b**) device after removal of the rigid housing; (**c**) aging condition (red circle); (**d**) the power supply surface after removal of the sealing compound.

Figure 5 shows the photograph and infrared spectroscopy result of the purple soft elastomer material used in the circuit part protection. Figure 5a presents the photograph of the aged elastomer, where the red circle highlights the region with visible void defects. The spectrum in Figure 5b indicates that the sample is mainly composed of perfluoropolymer, whose gas leak rate is usually below 1×10^{-10} Pa·l/s at room temperature. This material is designed for circuit protection and does not possess the structural function to maintain an ultra-high vacuum [26]. For the devices that completely lost image on the screen (Samples No. 3, No. 4, and No. 6, which failed to undergo performance parameter testing after 6 and 12 months of exposure), baking and retesting are carried out in a high vacuum and temperature chamber. It is found that the devices had completely failed. Subsequently, the devices are disassembled and inspected.

Figure 6a–d show the physical view of the image intensifier tube shell and the microscopic morphology of the tube shell sealing interface. Cracks are observed on the phenolic resin rigid housing on the device surface, and obvious gaps exist between the internal soft elastomer filler and the tube shell. Figure 6b provides a low-magnification overview of the sealing interface, while Figure 6c,d present the magnified view that clearly reveals these

interfacial gaps marked by the colored circle. Further helium leak testing is performed on the tube shell and ceramic ring responsible for maintaining the vacuum level of the image intensifier. Figure 6e is the schematic diagram of gas leak rate detection. The hermeticity of the image intensifier tube shells is evaluated using a helium mass spectrometer leak detector with a detection limit of 1×10^{-13} Pa·l/s. The test followed the standard practice described in ASTM E1603 [27]. It is found that the ceramic ring of this device had a clear gas leak problem, with a gas leak rate reaching as high as 2.4×10^{-11} Pa·l/s. Considering the volume of the image intensifier, theoretically, the vacuum level drops to 1×10^{-4} Pa in just three months, meaning that the theoretical lifetime of the device would not exceed three months.

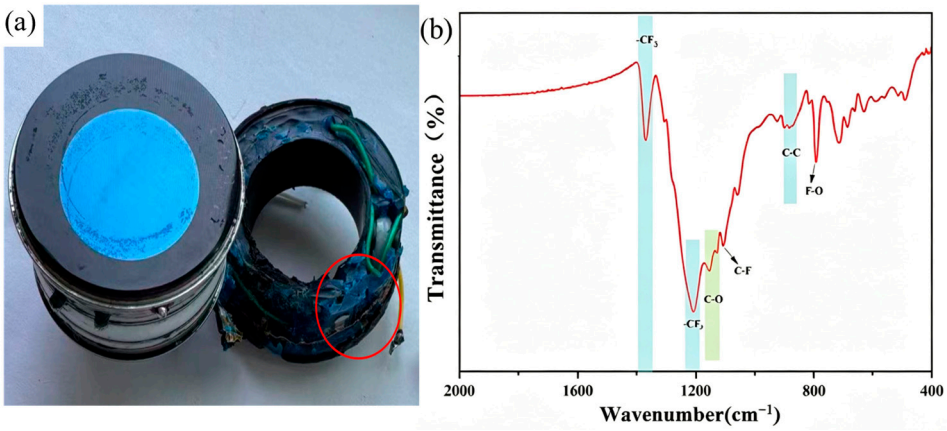


Figure 5. Attenuated total reflection (ATR) infrared spectroscopy test results of the circuit part and the green soft elastomer. (**a**) Morphology of the circuit part; (**b**) infrared spectroscopy result of the green elastomer.

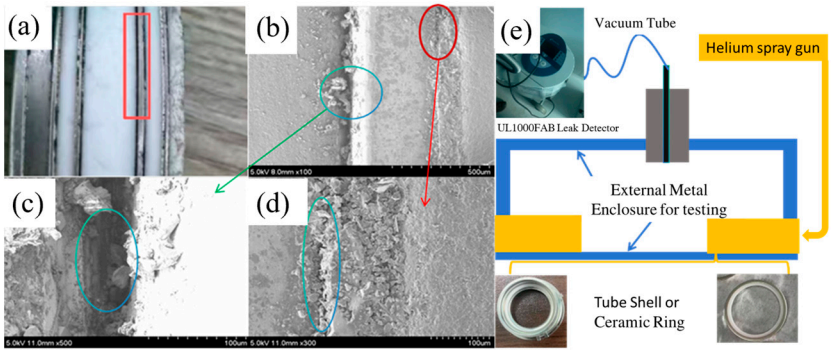


Figure 6. Physical and micro-morphology of the tube shell for sample 4# and gas leak rate detection. (**a**) Photograph of the tube shell; (**b**) low-magnification overall morphology of the sealing interface (scale bar: 500 μm); (**c**) local magnification of the interface edge (scale bar: 100 μm); (**d**) local magnification of the central region of the interface (scale bar: 100 μm); (**e**) schematic diagram of gas leak rate detection.

For the devices exhibiting no obvious defects but showing gain performance degradation, baking and retesting, as well as disassembly analysis are carried out. It is found that after baking in a high vacuum and temperature chamber, when key parameters such as luminance gain are re-measured, some devices show a significant improvement in parameters, including luminance gain, under an operating current of 29 mA, with no flickering or other field-of-view defects observed. The luminance degradation of the devices is irreversible under high temperature (Figure 3b), yet reversible under high vacuum. This further confirms that moisture ingress serves as the main cause for the performance decay of image intensifiers. The presence of numerous cracks, voids, and delamination between

the ceramic ring, the ceramic material, and the metal spacer inside the image intensifier is the direct cause of the potentially high gas leak rate of the product. Due to the high gas leak rate, the ingress of moisture and oxygen from the atmosphere into the device interior leads to a decrease in internal vacuum, which is the main mechanism responsible for the luminance gain degradation and even failure of the image intensifier.

3.4. Vacuum Degradation Simulation

Based on the flow characteristic model for small leak holes, the gas flow rate in tube shells can be quantified. Owing to the complexity of tube shell fabrication, parameter fluctuations inevitably emerge during manufacturing. Therefore, the numerical parameters are set as follows: membrane porosity (10^{-3}–10^{-10}), exposed area (10^{-3}–10^{1} cm^2), pore diameter (1 nm–2000 nm), channel length (1–3 mm), and typical gas species (H_2, CO, O_2, H_2O and CO_2) and pressure difference 10^5 Pa. The calculation results reveal that the achievable gas leak rate ranges from 10^{-19} Pa·l/s to 10^{-3} Pa·l/s. So, during the manufacturing process of image intensifiers, these micro-leak holes may result in the deterioration of the internal vacuum of the image intensifier.

Based on the model of outgassing characteristics of internally dissolved gases in tube shell materials, the one-dimensional transient hydrogen diffusion simulation based on this model was carried out at a constant temperature of 723 K for austenitic stainless steel. The parameters are assumed as follows: D_0 is equal to 3.64×10^{-2} cm^2s^{-1}, E_b is equal to 60 kJ·mol^{-1}, and K_r is equal to 3.41×10^{21} $cm^4 \cdot s^{-1}$. During isothermal annealing, the hydrogen outgassing rate starts at a high level of about 10^{12} molecules·$cm^{-2}s^{-1}$ and decays rapidly in the early stage as shown in Table 2. As annealing proceeds, the decay slows and the outgassing rate decreases gradually over time. After 10^5 s of annealing at 723 K, the instantaneous hydrogen outgassing rate falls below 10^9 molecules·$cm^{-2}s^{-1}$. Upon cooling to room temperature, bulk-hydrogen depletion and the strong suppression of diffusion and surface recombination at low temperature jointly lead to a 5–6-orders-of-magnitude reduction in the tube-shell outgassing rate. According to the simulation results, after vacuum heat treatment, the outgassing rate of gases dissolved in the metal inside the image intensifier is 10^{-17} Pa·l/(cm^2·s). Consequently, the time required for the internal vacuum level to degrade from 10^{-9} Pa to 10^{-4} Pa is at least 400,000 h (approximately 46.3 years for the inner surface area less than 30 cm^2). Furthermore, during the manufacturing process of the image intensifier, all components of the tube are subjected to vacuum heat treatment under the same conditions; after such treatment, the outgassing of dissolved gases from the materials should exhibit good consistency. Therefore, the outgassing of dissolved gases from the tube shell after vacuum heat treatment is not the primary cause of vacuum degradation in the image intensifier.

Table 2. Relationship between material outgassing rate and time during high-temperature degassing at 723 K.

Annealing Time (s)	**10**	**10^3**	**10^4**	**5×10^4**	**10^5**
Q (mole·cm^{-2}·s^{-1})	1.4×10^{12}	4.8×10^9	2.8×10^9	9.1×10^8	7.8×10^8

A model was established for the relationship between the tube shell gas leak rate and internal vacuum. Based on this model, the curves of vacuum level as a function of time under these five different gas leak rates are plotted, as shown in Figure 7. The gas leak rates are set to 10^{-16} Pa·l/s, 10^{-15} Pa·l/s, 10^{-14} Pa·l/s, 10^{-13} Pa·l/s, and 10^{-12} Pa·l/s, respectively. It is assumed that the volume of the image intensifier is 1 cm^3, the initial vacuum level of the image intensifier can reach 10^{-8} Pa [14], and the time range is 100,000 h. According to the vacuum decay kinetic model (Equation (6)), the time required for the internal vacuum

level of the image intensifier to drop from the initial value $P_0 = 1 \times 10^{-8}$ Pa to the failure threshold $P_t = 1 \times 10^{-4}$ Pa is calculated for five different gas leak rate conditions. The calculation assumed an effective internal volume of the image intensifier V = 1 cm^3 = 1×10^{-3} L. The calculated results are converted from seconds to hours (1 h = 3600 s), yielding the durations under different gas leak rates, which are directly presented by the labeled points in Figure 7.

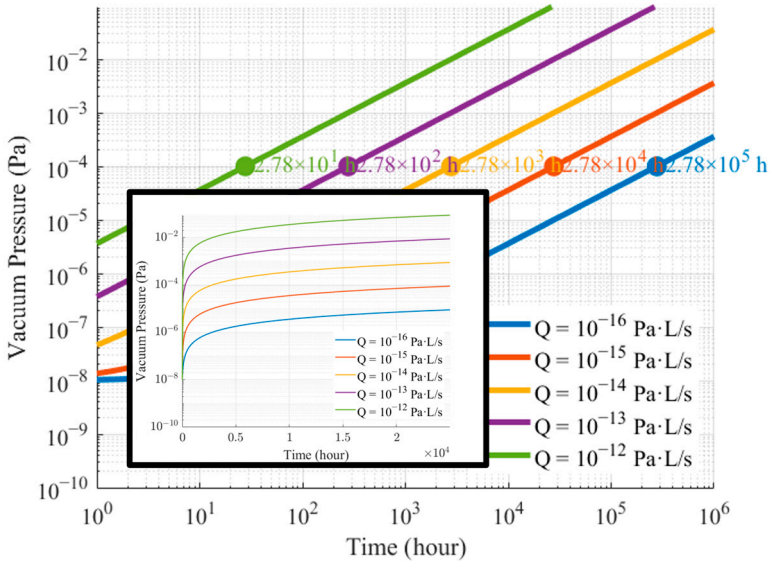


Figure 7. Vacuum level decay under different gas leak rates (log–log plot, initial vacuum level is 1×10^{-8} Pa), the insert is a semi-log plot.

The simulation results further reveal that, assuming an initial vacuum level of $P_0 = 1 \times 10^{-8}$ Pa, the vacuum level decreases rapidly in the initial stage as storage time increases, and then tends to stabilize. Moreover, the higher the gas leak rate, the faster the initial decay rate of the internal vacuum level of the tube shell, and the lower the stabilized vacuum level. Therefore, when manufacturing image intensifier products, the production units should strive to minimize micro-leak holes in the image intensifier, thereby reducing the gas leak rate and ensuring an optimal internal vacuum, which is beneficial for extending the lifetime of the image intensifier.

3.5. Influence of Water Vapor Concentration on Luminance Gain

Figure 8 shows the normalized luminance gain degradation values and their mean values of five image intensifiers after 50 h of storage under varying water vapor concentrations. The five image intensifiers used in the experiment include two third-generation image intensifiers (Third-Gen II) and three multi-alkali photocathode image intensifiers (MA II). Relevant storage conditions for each concentration are indicated in the figure. All data group were collected from samples stored in a temperature–humidity chamber, with water vapor concentrations of 8.4, 62.9 and 118.05 g/m^3, respectively. The maximum deviations in individual measurements from the corresponding averages are 0.0024, 0.0540 and 0.0920, while the relative standard deviations (RSD) reach 0.1%, 4.4% and 5.9%, respectively. It is evident that the degradation rate of the screen luminance gain of image intensifiers is proportional to water vapor concentration. The empirical formula for the luminance gain degradation of the image intensifier as a function of water vapor concentration can be derived as Formula (13):

$$\frac{G_0 - G}{G_0} = k \times a \tag{13}$$

where G_0 is the initial luminance gain; G is the luminance gain after a certain exposure time; a is the water vapor concentration (absolute humidity, g/m^3); and k is the attenuation coefficient (1.75×10^{-3} m^3/g for 50 h), which depends on factors such as material properties, exposure time, and temperature (unit: m^3/g). It can be further rearranged as:

$$G = G_0\left(1 - k \times \frac{RH \cdot E(T) \cdot M}{RT}\right) \tag{14}$$

According to the graphical analysis of the luminance gain degradation data of image intensifiers exposed in the field for 24 months, the luminance gain performance degradation shows a linear relationship during the first 12 months, and then becomes essentially stable. This indicates that after the device is moved from a vacuum packaging environment to a high-temperature and high-humidity environment, the luminance gain performance decreases linearly with the ingress of water vapor in the initial stage. After degrading to a certain value and after 12 months, the vacuum level inside the image intensifier begins to stabilize, and the water vapor concentration remains at around 14 g/m^3 (annual average temperature 20 °C, average relative humidity 69%), as shown in Figure 9. The above phenomenon indicates that the water vapor pressure difference between the inside and outside of the device is no longer sufficient to further degrade the performance of the core internal components, demonstrating that the influence of water vapor concentration on the core components tends to stabilize after it increases to a certain level.

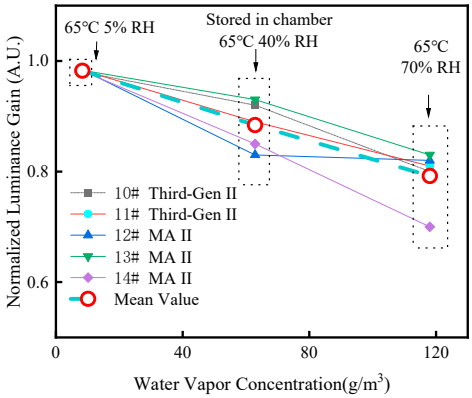


Figure 8. Relationship between the luminance degradation value of the image intensifiers screen and water vapor concentration.

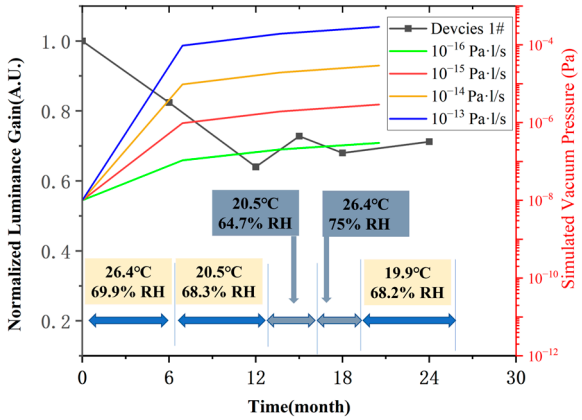


Figure 9. Luminance degradation of the image intensifier as a function of exposure time under natural humid and hot environments; the inset illustrates the variation trend of vacuum degree inside the image intensifiers after 12 months under different gas leak rates.

Consistent with our initial hypothesis that sealing defects dominate internal vacuum deterioration, this work identifies ceramic–metal interfacial micro-defects as the primary driver of moisture ingress and luminance gain loss, aligning well with classical leakage theories for vacuum electronic devices. These findings delineate the complete failure cascade and provide quantitative guidance for ceramic packaging optimization to enhance environmental adaptability. Future research will investigate how different tube shell fabrication processes affect sealing reliability, to extend the generalizability of the proposed degradation model.

4. Conclusions

This study systematically analyzes the failure mechanism and performance evolution law of image intensifiers under humid and hot environments. Experimental and modeling results show that micro-defects in the ceramic ring and its interfaces within the packaging structure are the root cause of leakage and internal vacuum degradation. The ingress of moisture and air under high-temperature and high-humidity conditions significantly exacerbates this process. It is experimentally demonstrated that the degradation rate of luminance gain is highly correlated with humidity and can be quantitatively predicted by establishing a relationship between gas concentration and performance change. This study identifies the primary external driving factor restricting the service life of devices in humid and hot environments, and verifies that differences in the gas leak rates of ceramic components fundamentally lead to variations in device lifetime. On this basis, optimizing the ceramic packaging process to reduce gas leakage is expected to improve the operational reliability and environmental resistance of image intensifiers.

Author Contributions: Conceptualization, M.L. and M.Z.; methodology, M.Z. and D.S.; software, W.C. and D.S.; validation, M.X. and R.Y.; formal analysis, M.Z. and M.L.; investigation, M.Z.; resources, D.S.; data curation, M.X.; writing—original draft preparation, M.Z.; writing—review and editing, R.L. and D.S.; visualization, M.L.; supervision, W.C. and D.S.; project administration, W.C. All authors have read and agreed to the published version of the manuscript.

Funding: This work was supported by the National Defense Science, Technology and Industry Bureau (JSHS2023208S001).

Data Availability Statement: The data that support the findings of this study are available from the corresponding author upon reasonable request.

Conflicts of Interest: The authors declare no conflicts of interest.

References

1. Shi, J.; Wang, S.; Sun, Y.; Xie, Q. Third generation of image intensifier brightness gain measurement device. *J. Appl. Opt.* **2011**, *32*, 300–302.
2. Fukasawa, A.; Kamiya, A.; Muramatsu, S.; Negi, Y.; Suyama, M. High-performance HPD for photon counting. In *Proc. SPIE 8033, Advanced Photon Counting Techniques V*; SPIE: Bellingham, WA, USA, 2011; Volume 8033, p. 80330S.
3. Fukasawa, A.; Haba, J.; Kageyama, A.; Nakazawa, H.; Suyama, M. High speed HPD for photon counting. *IEEE Trans. Nucl. Sci.* **2008**, *55*, 758–762. [CrossRef]
4. Li, X.; Chang, L.; Zhao, H.; Qiu, Y.; Chen, J.; Zhang, Y. Comparison of resolution between super Gen. II and Gen. III image intensifier. *Acta Photonica Sin.* **2021**, *50*, 0904003.
5. Karkare, S.; Boulet, L.; Cultrera, L.; Dunham, B.; Liu, X.; Schaff, W.; Bazarov, I. Ultrabright and ultrafast III-V semiconductor photocathodes. *Phys. Rev. Lett.* **2014**, *112*, 097601. [CrossRef] [PubMed]
6. Ohnuki, T.; Michalet, X.; Tripathi, A.; Weiss, S.; Arisaka, K. Development of an ultra-fast single-photon counting imager for single-molecule imaging. In *Proc. SPIE 6092, Ultrasensitive and Single-Molecule Detection Technologies*; SPIE: Bellingham, WA, USA, 2006; Volume 6092, p. 60920.
7. Feng, D.; Guo, X.; Bai, X.; Zhang, Q.; Dang, X.; Zhang, S.; Yang, S.; Li, Q.; Han, K. Effect of Luminance Gain on Image Quality of Third Generation Low-Light-Level Image Intensifier. *Infrared Technol.* **2023**, *45*, 188–194.

8. Chrzanoski, K.; Stafiej, B. Objective method of measuring resolution of image intensifier tubes. *Metro Meas. Syst.* **2024**, *31*, 339–352. [CrossRef]
9. Bai, X.; Guo, H.; Yang, S.; Shi, F.; Hu, Z.; Hou, Z.; Chen, X.; Huang, W. Luminance Gain Measurement and Life Prediction of Low-Light-Level Image Intensifier. *Infrared Technol.* **2019**, *41*, 203–207.
10. Zeng, J.; Yang, Q.; Gong, Y.; Li, T.; Wang, Y.; Li, X.; Zhao, H.; Ma, H.; Xu, C.; Wu, Y.; et al. Study on the Influence of Performance with the Working Time in the Super Gen-II Image Intensifier. *Infrared Technol.* **2023**, *45*, 869–875.
11. Zhao, H.; Liu, X.; Chen, C.; Xu, W.; Xie, J.; Zhang, Z.; Jiang, Z.; Xu, X.; He, Z.; Shu, R.; et al. Development and testing of a novel microstrip photocathode ICCD for lunar remote Raman detection. *Sensors* **2025**, *25*, 1528. [CrossRef] [PubMed]
12. Chanlek, N.; Herbert, J.; Jones, R.; Jones, L.B.; Middleman, K.J.; Militsyn, B.L. The degradation of quantum efficiency in negative electron affinity GaAs photocathodes under gas exposure. *J. Phys. D Appl. Phys.* **2014**, *47*, 055110. [CrossRef]
13. Pavlenko, V.; Liu, F.; Hoffbauer, M.; Moody, N.A.; Batista, E.R. Kinetics of alkali-based photocathode degradation. *AIP Adv.* **2016**, *6*, 115008. [CrossRef]
14. Guo, X.; Pang, Y.; Deng, N.; Yuan, Y.; Hu, W.; Bu, R.; Dong, M.; Chen, L. Outgassing characteristics of ceramic shell material and microchannel plates of third-generation low-light-level image intensifiers. *J. Phys. Conf. Ser.* **2023**, *2468*, 012110. [CrossRef]
15. Yao, Z.; Pang, Y.; Yuan, Y.; Hu, W.; Bu, R.; Fan, H. Numerical simulation of outgassing characteristics of microchannel plate glass. *AIP Adv.* **2021**, *11*, 075015. [CrossRef]
16. Paquet, A.; Deshaies, S.; Desroches, Y.; Whalin, J.; Topart, P. Influence of ceramic package internal components on the performance of vacuum sealed uncooled bolometric detectors. In *Proc. SPIE 8614, Reliability, Packaging, Testing, and Characterization of MOEMS/MEMS and Nanodevices XII 2013*; SPIE: Bellingham, WA, USA, 2013; Volume 8614, p. 86140G.
17. Wisniewski, P.; Sitek, R.; Towarek, A.; Choinska, E.; Moszczynska, D.; Mizera, J. Molding Binder Influence on the Porosity and Gas Permeability of Ceramic Casting Molds. *Materials* **2020**, *13*, 2735. [CrossRef] [PubMed]
18. Dionet, C.; Perosevic, G.; Javier, J.; Fernandez, S.; Hurdle, T.; Moradi, M.; Neely, A.; Ma, K.; Albarghouti, M. Dark Current Leakage in Optoelectronic Hermetic Packages. In *Proc. International Symposium on Optical Memory (ISOM)*; International Microelectronics Assembly and Packaging Society: Pittsburgh, PA, USA, 2017; Volume 2017, pp. 669–674.
19. Yuan, J. Mechanisms for Gas Diffusion and Flow Through Shale with Water Saturation. Master's Thesis, University of Calgary, Calgary, AB, Canada, 2022.
20. Jo, Y.; Kim, D.; Wang, J.; Oppenheim, J.J.; Dincă, M. Humidity-Mediated Dual Ionic−Electronic Conductivity Enables High Sensitivity in MOF Chemiresistors. *J. Am. Chem. Soc.* **2024**, *146*, 20213−20220. [CrossRef] [PubMed]
21. Yang, Y.; Liu, J.; Zhou, X.; Zhao, H.; Liu, Y.; Wang, C.; Zhao, Y.; Ge, F.; Xiao, J.; Luo, R.; et al. Environmental Adaptability of Infrared Antireflection Films in Humid Hot Rain Forest. *Infrared Technol.* **2021**, *43*, 1197–1201.
22. Qian, Y.; Chang, B.; Qiu, Y.; Tang, J.; Zhang, J.; Chen, H. Measurement of Luminance Gain and Equivalent Background Input in LLL Image Intensifiers. *Vac. Electron.* **2004**, *2*, 34–37.
23. Roy, S.; Raju, R. Modeling gas flow through microchannels and nanopore. *J. Appl. Phys.* **2003**, *93*, 4870–4879. [CrossRef]
24. Zheng, H.; Liu, P. Analyses of ceramic material gassing property. *Vac. Electron. Technol.* **2001**, *6*, 28–30.
25. Akaishi, K.; Funato, Y. Simulation of Hydrogen Outgassing in Ultrahigh Vacuum Chamber and Fusion Device by Recombination Limited Model. *J. Vac. Sci. Technol. A* **2002**, *20*, 848–856. [CrossRef]
26. Vega Puga, E.; Brendelberger, S.; Pierno, F.; Wischek, J.; Sattler, C. Sealability analysis of aged elastomer O-rings for usage in solar thermochemical water-splitting reactors. *Key Eng. Mater.* **2025**, *1007*, 37–48. [CrossRef]
27. *ASTM E1603/E1603M-11*; Standard Practice for Leakage Measurement Using the Mass Spectrometer Leak Detector or Residual Gas Analyzer in the Hood Mode. ASTM International: West Conshohocken, PA, USA, 2017.

Disclaimer/Publisher's Note: The statements, opinions and data contained in all publications are solely those of the individual author(s) and contributor(s) and not of MDPI and/or the editor(s). MDPI and/or the editor(s) disclaim responsibility for any injury to people or property resulting from any ideas, methods, instructions or products referred to in the content.